

# Globularity-Selected Large Molecules for a New Generation of Multication Perovskites

Somayeh Gholipour, Abdollah Morteza Ali,\* Juan-Pablo Correa-Baena, Silver-Hamill Turren-Cruz, Fariba Tajabadi, Wolfgang Tress, Nima Taghavinia, Michael Grätzel, Antonio Abate, Filippo De Angelis, Carlo Alberto Gaggioli, Edoardo Mosconi, Anders Hagfeldt,\* and Michael Saliba\*

Perovskite solar cells (PSCs) use perovskites with an  $APbX_3$  structure, where A is a monovalent cation and X is a halide such as Cl, Br, and/or I. Currently, the cations for high-efficiency PSCs are Rb, Cs, methylammonium (MA), and/or formamidinium (FA). Molecules larger than FA, such as ethylammonium (EA), guanidinium (GA), and imidazolium (IA), are usually incompatible with photoactive “black”-phase perovskites. Here, novel molecular descriptors for larger molecular cations are introduced using a “globularity factor”, i.e., the discrepancy of the molecular shape and an ideal sphere. These cationic radii differ significantly from previous reports, showing that especially ethylammonium (EA) is only slightly larger than FA. This makes EA a suitable candidate for multication 3D perovskites that have potential for unexpected and beneficial properties (suppressing halide segregation, stability). This approach is tested experimentally showing that surprisingly large quantities of EA get incorporated, in contrast to most previous reports where only small quantities of larger molecular cations can be tolerated as “additives”. MA/EA perovskites are characterized experimentally with a band gap ranging from 1.59 to 2.78 eV, demonstrating some of the most blue-shifted PSCs reported to date. Furthermore, one of the compositions,  $MA_{0.5}EA_{0.5}PbBr_3$ , shows an open circuit voltage of 1.58 V, which is the highest to date with a conventional PSC architecture.

Organic–inorganic halide perovskites have an  $ABX_3$  structure, where A = rubidium (Rb), cesium (Cs), methylammonium (MA), and/or formamidinium (FA);<sup>[1,2]</sup> B = Pb or  $Sn$ ;<sup>[3]</sup> and X = Cl, Br, or I.<sup>[4]</sup> They hold much promise for photovoltaics because they combine high power conversion efficiencies (PCEs) at low processing costs. One recent development to improve the optoelectronic properties of perovskites is to use more and more complex perovskites with multiple cations. In the following, we analyze the suitability of the next larger cations to FA for multication engineering, i.e., ethylammonium (EA)  $[(C_2H_5)NH_3]^+$ , guanidinium (GA)  $[C(NH_2)_3]^+$ , and imidazolium (IA)  $[C_3N_2H_5]^+$ .<sup>[5]</sup>

Through modeling and calculations, we show that EA is compatible with high-performance 3D perovskites. We then conduct experimental film and device characterization on MA/EA perovskites of the form  $MA_{(1-x)}EA_xPb(I_{(1-y)}Br_y)_3$  (with  $x, y = 0-1$ ) spanning a band gap range

S. Gholipour, Dr. J.-P. Correa-Baena, Prof. A. Hagfeldt  
École Polytechnique Fédérale de Lausanne  
Laboratory of Photomolecular Science  
Station 6, CH-1015 Lausanne, Switzerland  
E-mail: anders.hagfeldt@epfl.ch

S. Gholipour, Dr. A. M. Ali  
Department of Physics  
Alzahra University  
Tehran 1993891176, Iran  
E-mail: mortezaali@alzahra.ac.ir

S.-H. Turren-Cruz  
Benemérita Universidad Autónoma de Puebla  
CIDS  
Av. San Claudio y 18 Sur  
Col. San Manuel  
Ciudad Universitaria  
CP 72570, P.O. Box 1067, Puebla, Pue. 7200, Mexico

Dr. F. Tajabadi  
Department of Nanotechnology and Advanced Materials  
Materials and Energy Research Centre  
Karaj 31787-316, Iran

Dr. W. Tress, Prof. M. Grätzel, Dr. A. Abate, Dr. M. Saliba  
École Polytechnique Fédérale de Lausanne  
Laboratory for Photonics and Interfaces  
1015 Lausanne, Switzerland  
E-mail: michael.saliba@epfl.ch

Prof. N. Taghavinia  
Department of Physics  
Sharif University of Technology  
Tehran 14588, Iran

Prof. N. Taghavinia  
Institute for Nanoscience and Nanotechnology  
Sharif University of Technology  
Tehran 14588, Iran

DOI: 10.1002/adma.201702005

from 1.59 to 2.78 eV. We provide ultraviolet–visible (UV–vis), photoluminescence (PL), scanning electron microscopy (SEM), X-ray diffraction (XRD), photovoltaic device testing, electroluminescence (EL), incident-photon-to-current-efficiency (IPCE), long term device stability, and density functional theory (DFT) calculations. These results are within the “bluest” region for working perovskite solar cells (PSCs) providing a new pathway toward this very important band gap region.<sup>[6,7]</sup> The (MA)<sub>0.5</sub>(EA)<sub>0.5</sub>PbBr<sub>3</sub> composition showed one of the highest reported open-circuit voltages ( $V_{oc}$ ) for PSCs at 1.58 V (1.63 V when cooled to  $-10$  °C and 5 sun illumination).

The suitability for a cation to be compatible with a high-performance, “black phase” 3D-perovskite can be assessed with the Goldschmidt tolerance factor<sup>[8]</sup>  $t = [R_A + R_X]/[\sqrt{2}(R_B + R_Y)]$ , where  $R_A$ ,  $R_B$ , and  $R_X$  are the perovskite constituents’ ionic radii. Empirically, “black phase” 3D perovskites tend to form when  $0.8 < t < 1.0$  is fulfilled. For molecules, this is the case for MA and FA with FA being the largest cation that still is suitable. Other molecules that are structurally similar to FA, but too large for black phase perovskites, are EA, GA, and IA.<sup>[5]</sup> We present this in **Figure 1a** (and Table S1, Supporting Information (SI)) where the tolerance factors is calculated based on effective ionic radii from refs. [5] and [9] for APbI<sub>3</sub> perovskite using Rb, Cs, MA, FA, EA, GA, and IA as cations (see Figure 1b for the molecular structures). The tolerance factors for Cs, MA, and FA are within the 3D perovskite “formation regime”. In our previous work, using a multiple cation approach, we show that Rb has a beneficial impact on the optoelectronic properties of the resulting perovskite films.<sup>[2]</sup> We note that EAPbI<sub>3</sub> and GAPbI<sub>3</sub> have tolerance factors exceeding 1. Interestingly, IAPbI<sub>3</sub> has a tolerance factor of 0.997, not far from FAPbI<sub>3</sub>, and therefore should have a black 3D structure. However, there are no reports on IA-based PSCs and we could not observe a black phase either when heating a film of IAPbI<sub>3</sub> (see Figure 1c for images taken at 100, 200, 300, and 400 °C). The same experiment was performed for EAPbI<sub>3</sub> and GAPbI<sub>3</sub>, and no black phase perovskite was observed. This is in contrast to CsPbI<sub>3</sub>, which forms a black perovskite upon heating above 335 °C.<sup>[10]</sup>

This indicates that the tolerance factor for more complex molecules than MA and FA needs revising. First steps to consider the nonspherical shape of the molecules were taken by Kieslich et al.,<sup>[5]</sup> which were used to the calculated tolerance factors in Figure 1a. However, this model is only accurate for elemental and simpler organic cations as is evident from the IAPbI<sub>3</sub> discrepancy (Figure 1a,c). More complex molecules on the other hand need additional considerations such as rigidity and molecular asymmetry (as well as chemical considerations like acidity).

Here, we revise the cationic radius by proposing the molecular globularity,  $g$ , defined as  $g = S/S_{eq}$ , where  $S$  is the actual

molecular surface and  $S_{eq}$  is the surface of a sphere of volume equal to the molecular volume. Notably,  $g$  increases from 1 as the molecular shape deviates from that of a sphere, accounting for molecular asymmetry. With the globularity factor, we define the tolerance factors (assuming a normalized tolerance factor of 1 for FA) of the cations (XA, with X = M, F, E, G, I) as  $t = 1 - [r_{eq}(FA)/g - r_{eq}(XA)/g]$  where  $r_{eq}$  is the radius of the sphere with the same volume as that calculated for the molecule. All modeling and calculation details (including DFT) are given in Supplementary Note S1 together with Figures S1 and S2 in the SI. In Figure 1a, we present revised tolerance factors showing that IA and GA fall out of range. Furthermore, our calculations confirm the expected tolerance factor trend where MA has a smaller tolerance factor than FA and EA. Also, the IA contradiction is resolved with IA now clearly falling out of range. GA, on the other hand, could still be in an accessible range, consistent with the report of partial GA incorporation in perovskite films.<sup>[11]</sup> The main surprise, however, is EA that is even closer to the black perovskite formation regime than previously anticipated (more so than even Rb on the other side of the range). This renders EA close to being a compatible with 3D perovskites and may thus be tolerated in large quantities. This has previously not been realized because EA never shows a black phase as it borders the tolerance factor range for 3D perovskites resulting in a distorted, nonblack phase lattice.

To visualize the different arrangement of the organic cations, we select a mixed MA<sub>0.75</sub>EA<sub>0.25</sub>PbI<sub>3</sub> (guided by device data from further below) compounds and report in **Figure 2** the electron density map of the EA and MA cations in the cuboctahedral perovskite cavity. We note, while MA preferentially lies along one of the two equivalent 110 directions (recall that in the tetragonal  $I4cm$  space group the 110 direction corresponds to the cubic 100 axis) with a slight angle with respect to the ab plane,<sup>[12]</sup> the C–N axis in the EA cation shows a deviation from the (110) direction exploiting also some space available along the (111) direction to accommodate the bulkier cation. The MA/EA exchange comes at the expense of a small energy penalty (of less than 0.1 eV per EA molecule), due in part to the loss in the optimal hydrogen bonding between the EA hydrogens (actually protons) and the negatively charge iodine atoms, which is instead maximized in MA (see SI for additional details).

Thus, after establishing EA (in contrast to GA, IA) as the closest candidate for 3D compatible perovskites, we proceed with experimental demonstration of EA-inclusion into full perovskite solar cell devices.

For this, we follow a mixing strategy where smaller cations are added to larger cations aiming for integration of large quantities of EA.<sup>[2,4,13]</sup> We note that previous reports show the usage of only small amounts of large cations as “additives”. For example, using large quantities of phenethylamine (PA) with

Dr. A. Abate  
Adolphe-Merkle-Institute  
University of Fribourg Ch. du. Musée 3  
CH-1700 Fribourg, Switzerland

Dr. F. De Angelis, C. A. Gaggioli, E. Mosconi  
Computational Laboratory of Hybrid/Organic Photovoltaics (CLHYO)  
CNR-ISTM  
via Elce di Sotto 8, I-06123 Perugia, Italy

Dr. F. De Angelis, C. A. Gaggioli, E. Mosconi  
CompuNet  
Istituto Italiano di Tecnologia  
Via Morego 30, 16163 Genova, Italy

 The ORCID identification number(s) for the author(s) of this article can be found under <https://doi.org/10.1002/adma.201702005>.

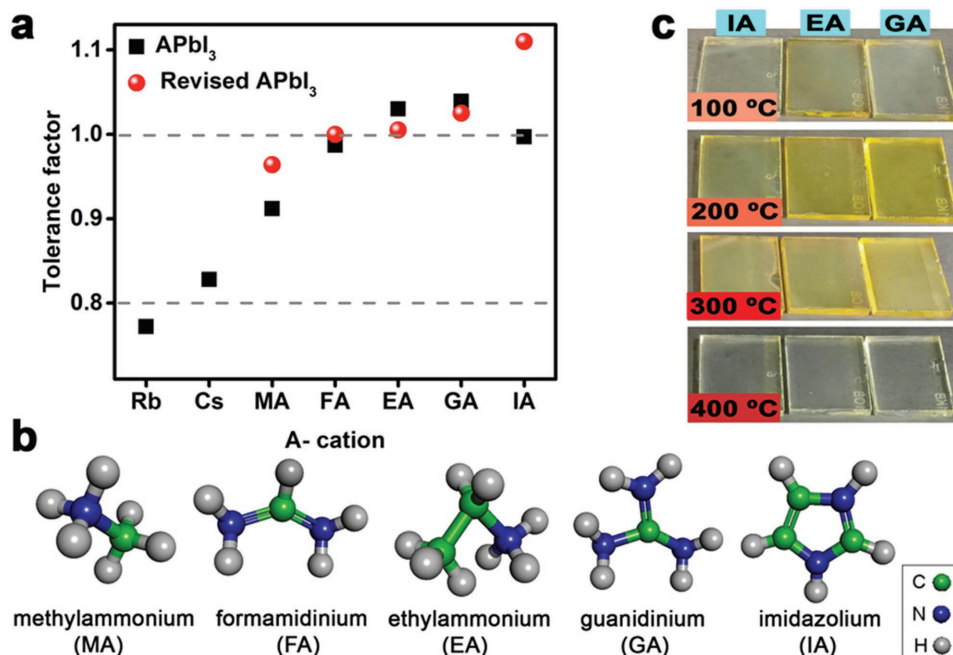


**Figure 1.** a) Tolerance factor of APbI<sub>3</sub> (squares) and revised APbI<sub>3</sub> (circles) that take “globularity” (related to the shape of the molecule) into account. Between the dashed lines, we find “established perovskites” suited for photovoltaics. b) 3D structure of the different organic amine cations. c) Heated IAPbI<sub>3</sub>, EAPbI<sub>3</sub>, and GAPbI<sub>3</sub> films at different temperatures at ambient atmosphere. Note that a “black phase” is never achieved with these “bulky” cations.

MA is detrimental for the optoelectronic properties of perovskite thin films and benefits mainly moisture resistance (the best performances correspond roughly to 1 PA molecule per 30 MA molecules).<sup>[14]</sup>

In the following, we thus investigate also MA/EA perovskites of the form MA<sub>(1-x)</sub>EA<sub>x</sub>Pb(I<sub>(1-y)</sub>Br<sub>y</sub>)<sub>3</sub> presenting film and device characterization.

In **Figure 3a,b**, a matrix comprised of MA<sub>(1-x)</sub>EA<sub>x</sub>Pb(I<sub>(1-y)</sub>Br<sub>y</sub>)<sub>3</sub> perovskites is shown illustrating the highly tuneable band gaps of PSCs. The EA content was changed from  $x = 0$  to 0.25 in each row and the Br content was changed from  $y = 0$  to 1 in each column; the nomenclature refers strictly to the stoichiometry of the precursor solution. The compositions with iodine as the exclusive halide are dark brown, and as the bromide

content increases they successively become more red. When the bromide content gets close to 70%, they get a clear yellow tone.

**Figure 4a–d** show absorption as a function of wavelength and band gap (determined by the onset of absorption spectrum) for different EA content are given for MA<sub>(1-x)</sub>EA<sub>x</sub>PbI<sub>3</sub> and MA<sub>(1-x)</sub>EA<sub>x</sub>PbBr<sub>3</sub> (the full matrix can be found in Figures S3 and S4). Regardless of the MA/EA-ratio, higher bromide content results in a wider band gap (see Figure S3). In addition, the halide ratio alters the shape of the absorption curve. With higher bromide content, close to 100%, the absorption onset gets sharper and a peak in the absorption indicative of excitonic absorption, as previously reported for bromide rich perovskites.<sup>[15,16]</sup> The excitonic peak can be seen regardless of the MA/EA-ratio (Figure S3). Moreover, in Figure 4 and Figure S4, the behavior upon changing the MA/EA-ratio is shown. The effect of cation exchange on absorption edge is considerably smaller, as illustrated in Figure S4. As the EA content increases, the absorption edge shifts to larger band gaps. This is regardless of I/Br-ratio: higher EA content results in a blueshift (see Figure 4 and Figure S4), which is consistent with Peng et al. who synthesized MA/EA single-crystals.<sup>[17]</sup>

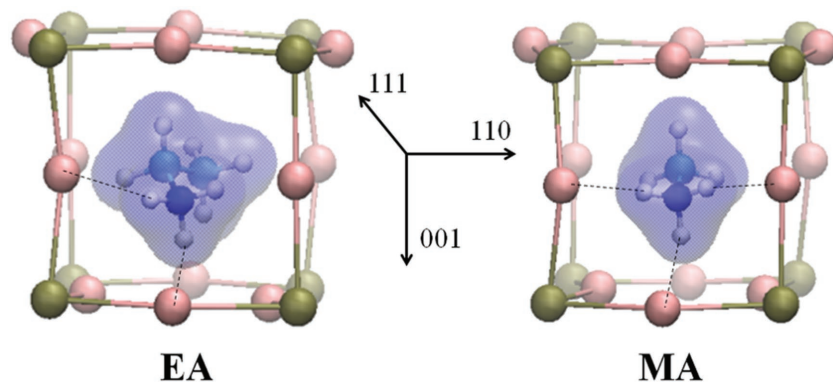


**Figure 2.** Electron density maps for EA and MA in the cuboctahedral perovskite cavity as calculated at their optimized geometries in MA<sub>0.75</sub>EA<sub>0.25</sub>PbI<sub>3</sub> compounds, along with the tetragonal crystal axes. Hydrogen bonds are shown as dashed lines, notice the different orientation of the EA and MA cation.

Analogously, in Figures S5 and S6, we show images of GA/MA and IA/MA mixtures with different concentrations of GA and IA. No continuous band gap shift was observed (unlike EA) which is consistent with larger cations not being tolerated in large quantities in 3D perovskites.<sup>[14]</sup>

Figure 4 also shows steady state PL data (dashed lines). For samples without or little

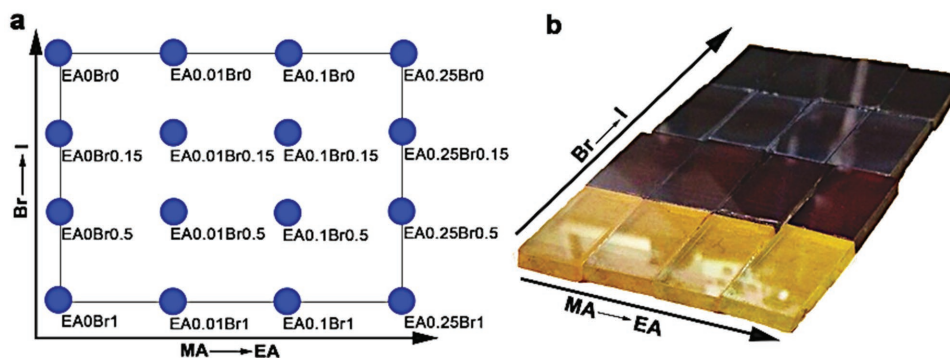


**Figure 3.** a) A graphical illustration and b) image of the investigated compounds. The perovskite compositions are of the form  $MA_{(1-x)}EA_xPb(I_{(1-y)}Br_y)_3$ . The columns depict an increase in iodine concentrations, the rows show an increase in EA.

Br, one distinct PL-peak centered around energies slightly higher than the band gap energy is observed. This would correspond to direct recombination from the conduction band edge to the valence band edge. For the pure Br perovskites, one PL-peak at the band gap energy is observed (see also Figure S7d). The peaks here are narrower than for the pure iodine perovskites confirming the more excitonic nature of the absorption for the bromide perovskites as observed in the absorption data. For films with more than 50% bromide, excluding the pure bromide perovskites, the PL spectra show more than one peak, as illustrated in Figure S7c. The peak at higher energies corresponds to the band edge recombination of the majority phase, but the peak at lower energies could be explained by phase separation with the formation of small amounts of a minority

phase, e.g., iodine rich perovskite-phase with a lower band gap. Such phase separation was reported by Jacobsson et al. for mixed cation (MA/FA), mixed halide (I/Br) systems.<sup>[18]</sup> For  $MA_{(1-x)}EA_xPbBr_3$ , as EA is increased, a continuous blueshift from 490 to 540 nm can be observed (see Figures S7 and S8b in Supplementary Note S2). This is a noteworthy result as it provides very precise fine-tuning in a highly relevant band gap region for display, light emitting device (LED), and laser applications (“green gap”). Moreover, shifting the band gap beyond  $MAPbBr_3$  poses a principled difficulty and requires cumbersome modifications. Using EA provides a convenient and novel solution to this challenge.

A typical trend in the PL-behavior, as the Br/I-ratio is varied, is illustrated in Figure S9. When the amount of bromide is

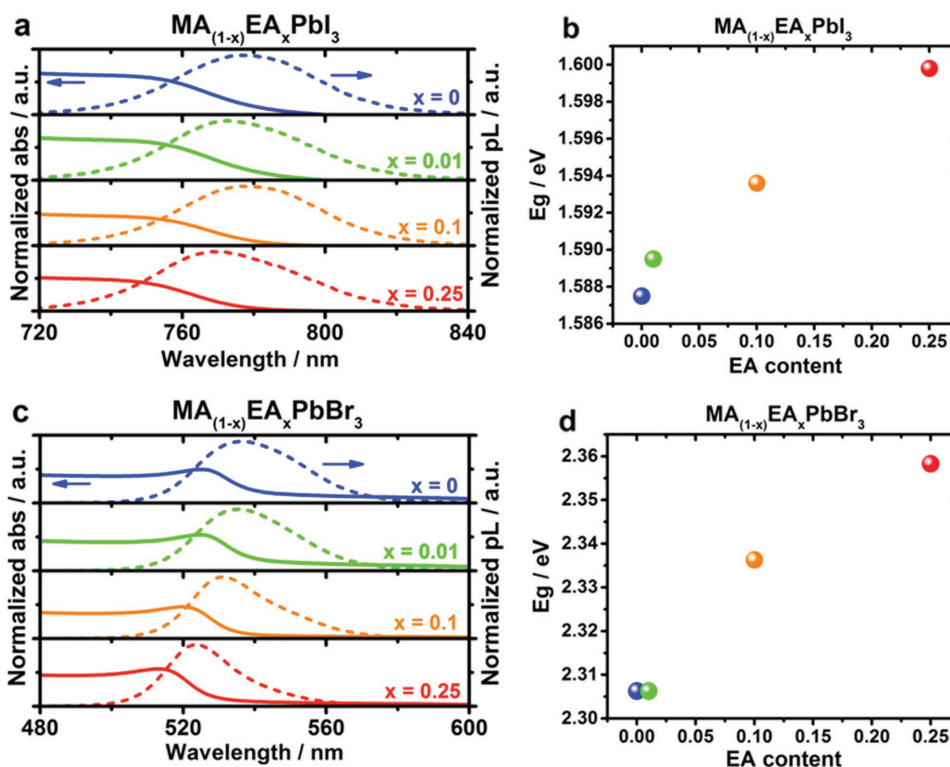


**Figure 4.** Normalized photoluminescence and optical absorption for a)  $MA_{(1-x)}EA_xPbI_3$  and c)  $MA_{(1-x)}EA_xPbBr_3$ , band gap for b)  $MA_{(1-x)}EA_xPbI_3$  and d)  $MA_{(1-x)}EA_xPbBr_3$ .

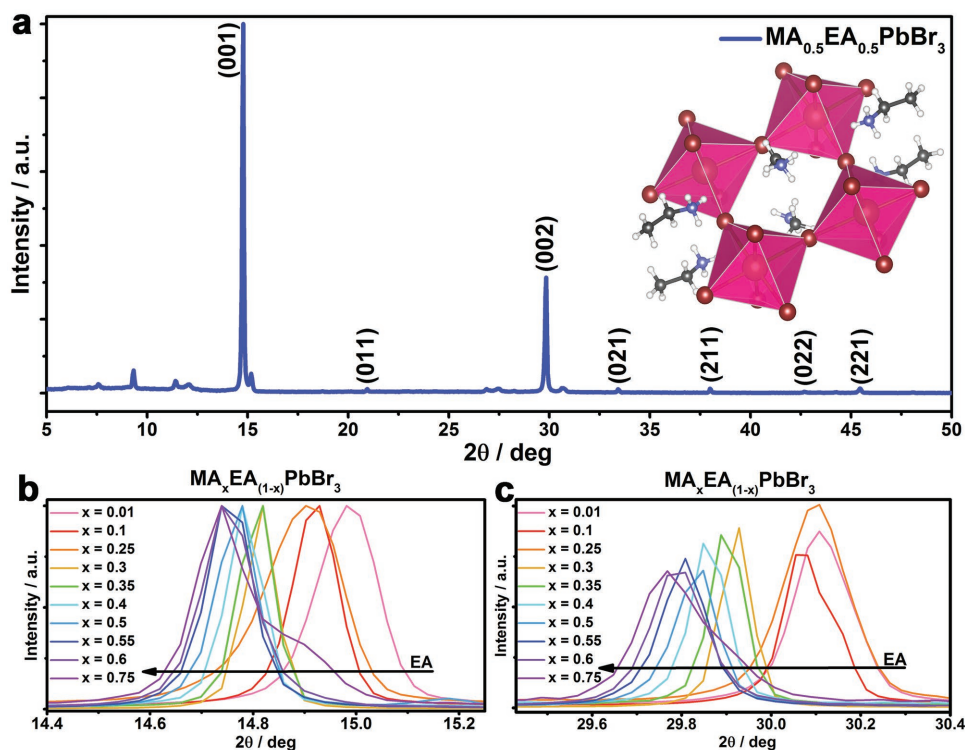


**Figure 5.** a) XRD data for  $\text{MA}_{0.5}\text{EA}_{0.5}\text{PbBr}_3$  compound (the inset shows the crystallographic structure for  $\text{MA}_{0.5}\text{EA}_{0.5}\text{PbBr}_3$ ). b) The (001) peak as a function of EA content for  $\text{MA}_{(1-x)}\text{EA}_x\text{PbBr}_3$ . c) The (002) peak as a function of EA content.

increased, there is a blueshift in the emission peak corresponding to the larger band gap. Also, for  $x = 0.25$  the PL seems slightly asymmetric, which could be due to light-induced halide segregation of the perovskite.<sup>[19]</sup> However, from Figure S8b, the asymmetric PL cannot be observed with large amounts of EA even for  $x = 0.75$ . Thus, high purity samples are verified and any additional phase or phase segregation cannot be observed from the PL data.

Another behavior of bromide rich perovskites is the narrower PL by increasing EA content as can be seen in Figure 4c. This may be attributed to more homogeneous film formation as shown in Supplementary Note S3 or could be related to EA aiding to form a more single-crystalline perovskite phase.<sup>[20]</sup>

We investigate the surface morphology of all compositions in Figure S10 and Supplementary Note S3 (where SEM images are shown). There are differences in morphology between the samples and it is not simple to discern a consistent trend. This observation is similar to our previously reported work on MA/FA mixtures.<sup>[18]</sup> In addition, SEM images for Br-rich compositions with different EA concentration are depicted in Figure S11. By increasing EA content, the grain boundaries disappear and more uniform films were formed.

XRD data were measured for all the different compositions. The full spectrum results for  $\text{MA}_{0.5}\text{EA}_{0.5}\text{PbBr}_3$  composition are given in Figure 5a. The full set of XRD patterns for  $\text{MA}_{(1-x)}\text{EA}_x\text{PbBr}_3$  compounds can be found in Figures S12 and S13 as well as Supplementary Note S4. The dominant phase for all the samples was the cubic crystal structure<sup>[21]</sup> with the exception of the  $\text{EAPbBr}_3$  sample. Since EA is larger than MA,<sup>[5,22]</sup> the unit cell is expected to expand

as EA replaces MA. In other words, the XRD data showing a shift of the “perovskite peak” (around  $15^\circ$  and  $30^\circ$ ) toward smaller angles is consistent with EA modifying the perovskite lattice for I- and Br-rich perovskites. According to Bragg’s law, a larger d-spacing shifts the diffraction peaks to smaller diffraction angles. This phenomenon is observed for both (001) and (002) reflections, as illustrated in Figure 5b,c. As shown in Table S4, the continuous shift is more ordered in (002) reflection ( $2\theta = 30^\circ$ ) than (001) reflection ( $2\theta = 15^\circ$ ). Also, we observe some phase separation in the PL spectra of the mixed halide Br/I perovskites (see Figure S7c). Such phase segregations can affect crystal lattice structure and correspondingly shift the XRD peak. In addition, new XRD peaks appeared beyond  $x = 0.3$  and  $2\theta$  lower than  $10^\circ$ , which had been observed recently by Stoumpos et al. who have shown that in 2D perovskites, the introduction of MA cations in the crystal structure reveal an additional low angle reflection for each added layer in  $(\text{BA})_2(\text{MA})_{n-1}\text{Pb}_{n-1}\text{I}_{3n+1}$  compounds.<sup>[23]</sup> Moreover, in the earlier works for MA/EA perovskites, the additional reflection peaks at angles lower than  $10^\circ$  are attributed to the smooth transition toward  $\text{EAPbBr}_3$ .<sup>[21]</sup> Therefore, these peaks are consistent with 2D perovskites. However, taking the shape of the molecular cation into account via the globularity factor, it can be better explained how EA is more compatible with a 3D structure than previously assumed (consistent with the terminology of a “quasi-3D” structure). Especially for small EA amounts, there is room for the lattice to expand and integrate EA. Beyond  $x = 0.3$ , EA starts to show more strongly in the perovskite composition as is consistent with the previous reports.<sup>[23]</sup> Also, we note that similar to the aforementioned MA/EA compositions, there is

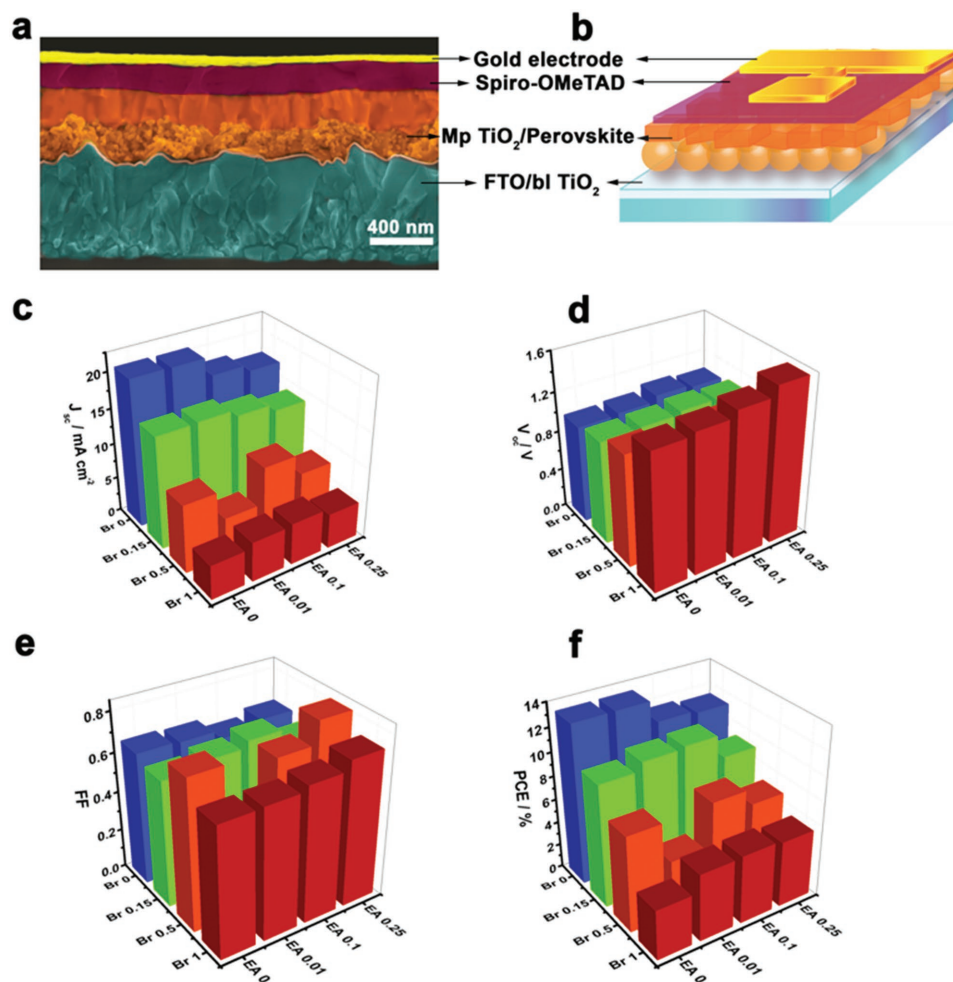


**Figure 6.** a) Cross-sectional scanning electron microscope (SEM) image of a device, b) device schematics, device performance parameters for different compositions. c)  $J_{sc}$ , d)  $V_{oc}$ , e) FF, and f) PCE.

some discrepancy between the precursor and film composition, which is an ongoing problem in the perovskite field.<sup>[24,25]</sup>

In addition, as shown in the PL spectra (Figure 4c) and top SEM images (Figure S11), the crystallinity increased for higher EA content in Br-rich perovskites exceeding 100 nm grain size (which is too large for XRD to measure the size accurately).

To understand the applicability of these novel compounds, solar cells were fabricated with MA/EA mixtures using a stack of fluorine-doped-tin-oxide (FTO)/compact-TiO<sub>2</sub>/meso-TiO<sub>2</sub>/perovskite/spiro-OMeTAD/Au.<sup>[2]</sup> We illustrate the stack in **Figure 6a,b** with an SEM cross-section image and corresponding schematics. PSCs were made with all 16 different compositions of MA/EA and I/Br, and the results are summarized in Figure 6c–f and in Table S5 (see Supplementary Note S5). The device performance shows that by increasing the Br/I-ratio, regardless of EA content, the  $V_{oc}$  increased. However, the short circuit current density ( $J_{sc}$ ) reduction results in PCE reduction. The trends of  $J_{sc}$  and  $V_{oc}$  can be explained by changes of the band gap (Figure 2 and Figure S8a). The trend of  $V_{oc}$  with maximum values approaching 1.6 V indicates that the charge transport layers such as the hole transport material (HTM) spiro-OMeTAD and TiO<sub>2</sub> are not fundamentally

restricting  $V_{oc}$ . More specifically, this indicates that the HTM in PSCs is not necessarily a major bottleneck.

Another striking attribute of these perovskites is their low non-radiative recombination rates compared to other thin film polycrystalline semiconductors. This property manifests itself in the relatively small difference between  $V_{oc}$  extracted from solar cells and their effective band gap potential ( $E_g/q$ ).<sup>[26]</sup> The best perovskite cells have relatively low values for the difference between band gap and  $V_{oc}$ ,  $E_g/q - V_{oc}$ , at around 400–450 mV.<sup>[27]</sup> This makes perovskites particularly interesting for high  $E_g$  cells in tandem cell stacks, where the high  $V_{oc}$  values give rise to substantial efficiency advantages. By device fabrication for different EA concentration in bromide rich compositions, we measure the difference between  $E_g/q$  and record  $V_{oc}$ , i.e., the “loss-in-potential” for these devices. **Figure 7a** and Table S6 show the loss in potential and energy band gap for different EA concentration in MA<sub>(1-x)</sub>EA<sub>x</sub>PbBr<sub>3</sub> compounds. The PL and UV spectra of these compounds are shown in Figure S8a,b. In Figure 7b, the PL spectra, together with absorption data, are given for the MA<sub>0.5</sub>EA<sub>0.5</sub>PbBr<sub>3</sub> compound, which has the lowest loss-in-potential with 788 mV.

In Figure 7c, we show the current density–voltage ( $J$ – $V$ ) curve and maximum power point tracking (MPP) of the highest

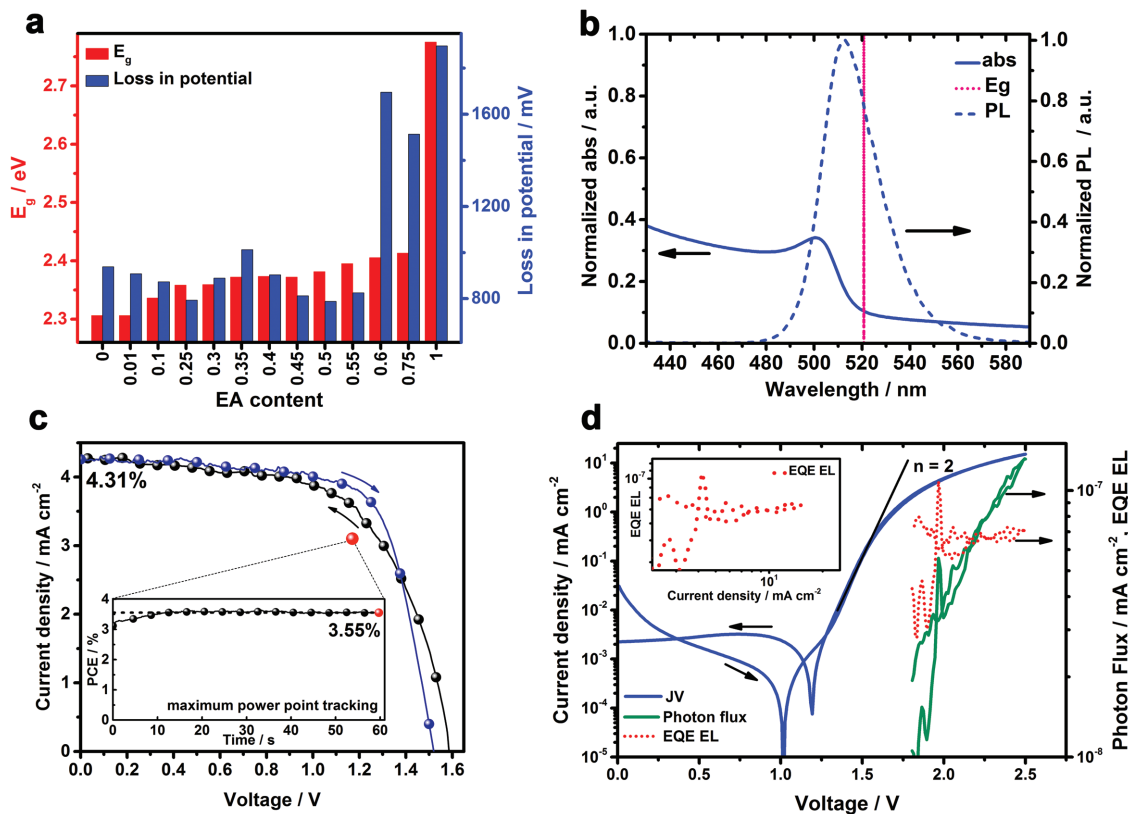


**Figure 7.** a) The loss in potential and energy band gap for different EA concentration in  $\text{MA}_{(1-x)}\text{EA}_x\text{PbBr}_3$  compounds. b) Normalized photoluminescence and optical absorption for  $\text{MA}_{0.5}\text{EA}_{0.5}\text{PbBr}_3$ , the band gap is illustrated by a vertical line. c) The  $J$ - $V$  curve of the champion mesoporous  $\text{TiO}_2/\text{MA}_{0.5}\text{EA}_{0.5}\text{PbBr}_3$  device taken at a scan rate of  $10 \text{ mV s}^{-1}$ , from forward bias (FB) to the short circuit condition (SC) and the reverse scan; the arrows indicate the  $J$ - $V$  scan direction. The inset shows the scan rate independent maximum power point (MPP) tracking for 60 s resulting in a stabilized efficiency of 3.55% at 1.17 V and  $3.1 \text{ mA cm}^{-2}$  (displayed as the red circles in the JV and MPP scan, respectively). d)  $J$ - $V$  curve ( $100 \text{ mV s}^{-1}$ , the arrows show the scan direction, blue), emitted photon flux expressed as voltage (green) and the  $\text{EQE}_{\text{EL}}$  (red) for  $\text{MA}_{0.5}\text{EA}_{0.5}\text{PbBr}_3$ . The inset shows the  $\text{EQE}_{\text{EL}}$  as a function of the electrical current density.

voltage  $\text{MA}_{0.5}\text{EA}_{0.5}\text{PbBr}_3$  device. The forward and reverse scan results are summarized in Table S7. We observe a  $V_{\text{oc}}$  of 1.58 V which is the highest recorded voltage for this device architecture to date. We also show different thickness dependences in Figure 6a and Figure S14 (including Table S8). This result is promising for water splitting applications that require high voltages and shows that the MA/EA compounds result in beyond state-of-the-art results.<sup>[28]</sup> We also observe independently the same high  $V_{\text{oc}}$  of 1.58 V on a planar  $\text{SnO}_2$  flat device (see Figure S15 and Table S7) confirming the perovskite film formation on flat substrates as well.

Furthermore, we measure the electroluminescence for a device with  $\text{MA}_{0.5}\text{EA}_{0.5}\text{PbBr}_3$  showing with 788 mV the lowest loss in potential of the series and a band gap of 521 nm (2.38 eV). The results obtained during a voltage sweep from 0 to 2.5 V and back are displayed in Figure 7d. The  $J$ - $V$  curve (blue) shows apart from resistive limits including hysteresis an exponential diode behavior with an ideality factor of  $\approx 2$  indicative for predominantly defect recombination. The hysteresis at lower voltages and the apparent  $V_{\text{oc}}$  in the dark are due to slow processes not having equilibrated during the  $J$ - $V$  scan.<sup>[29]</sup> An emitted photon flux (green) was detectable for  $>1.8 \text{ V}$ . Dividing it by the injection current, we obtain the external EL quantum

yield  $\text{EQE}_{\text{EL}}$  (red), which approaches  $7\text{e}-8$  and seems to be rather independent of the injection current. This value is equivalent<sup>[30]</sup> to a nonradiative loss in  $V_{\text{oc}}$  of 430 mV and therefore a total loss in potential of  $\approx 760 \text{ mV}$ , which is consistent with the photovoltaic measurements. Further work has to focus on reducing the nonradiative losses by optimizing the quality of the film and its interfaces to the charge transport layers.

For further evaluations of the contribution of EA to the photocurrent, we measure the IPCE of the  $\text{MA}_{(1-x)}\text{EA}_x\text{PbBr}_3$  compounds for  $x = 0$  to 0.75. The IPCE onset for  $\text{MA}_{(1-x)}\text{EA}_x\text{PbBr}_3$  blueshifted from 572 to 540 nm with an increased EA from  $x = 0$  to 0.75, as shown in Table S9 and Figure S16a. This is consistent with the continuous blue-tuning observed from PL measurements, as shown in Table S9 and Figure S16c. In addition, as shown in Figure S16b, the measured  $J_{\text{sc}}$  from the  $J$ - $V$  scan ( $4.28 \text{ mA cm}^{-2}$ ) and the integrated IPCE measurements ( $4.3 \text{ mA cm}^{-2}$ ) were in good agreement for the  $\text{MA}_{0.5}\text{EA}_{0.5}\text{PbBr}_3$  device.

In Figure S17, we also measured first aging data for  $\text{MA}_{0.5}\text{EA}_{0.5}\text{PbBr}_3$  for 45 h at room temperature under continuous illumination and maximum power point tracking in a nitrogen atmosphere. As the device ages, 72% of the initial performance is retained.

In summary, we introduced the concept of globularity as a measure to analyze large organic cation for suitable in multication perovskites. We realized that cations larger than FA were misclassified. This is especially the case for IA (reported as smaller) and EA (reported as larger). With this, we could show that EA in contrast to all other reported large cations can be incorporated in large quantities into 3D perovskites without being detrimental to the overall film quality.

We then investigated experimentally  $MA_{(1-x)}EA_xPb(I_{(1-y)}Br)_3$  (with  $x, y = 0-1$ ) perovskites spanning a band gap range from 1.59 to 2.78 eV. For  $MA_{(1-x)}EA_xPbBr_3$ , we observed a precisely fine-tunable band gap from 490 to 540 nm, a band gap region that is highly relevant for display, LED, and laser applications (“green gap”). Thus, EA provides a convenient and novel approach to access this most blueshifted region so far reported for working PSCs (not reachable with Br/I anions). Also, for the first time, an open circuit voltage close to 1.6 V for  $MA_{0.5}EA_{0.5}PbBr_3$  perovskite solar cell is observed—the highest voltage observed for this PSC architecture.

The identification and experimental implementation of EA as a 3D-compatible cation provides ample opportunities in a multication approach for synthesizing new perovskites with the potential for unexpected and beneficial properties.

## Experimental Section

**Fabrication of Perovskite Solar Cells:** Mesoporous  $TiO_2$  Substrate Preparation and Li-Doping: FTO glass sheets ( $10 \Omega^{-1}$ , Nippon Sheet Glass) were etched with zinc powder and HCl (4 M) to form a detached electrode pattern. Substrates were ultrasonically cleaned by a sequential 15 min 2% Hellmanex water solution, deionized water, ethanol, and acetone. Substrates were treated under UV-ozone for 15 min to remove the last traces of organic residues. A 30–50 nm thin compact  $TiO_2$  layer was then deposited on to the clean preheated substrates by spray pyrolysis from a precursor solution of titanium diisopropoxide bis(acetylacetonate) in anhydrous ethanol, using oxygen as the carrier gas on a hot plate set to 450 °C, followed by annealing at 450 °C, for 30 min in air. A mesoporous  $TiO_2$  layer was deposited by spin coating for 20 s at 4000 r.p.m. with a ramp of 2000 r.p.m., using 30 nm particle paste (Dyesol 30 NR-D) diluted in ethanol to achieve a 200 nm layer thickness ( $150 \text{ mg mL}^{-1}$ ). After the spin coating, the substrates were immediately dried at 100 °C for 10 min and then sintered again at 450 °C for 30 min under dry air flow.

Li-doping of mesoporous  $TiO_2$ <sup>[31]</sup> was accomplished by spin coating a 0.1 M solution of bis(trifluoromethylsulfonyl)imide lithium salt (Li-TFSI) in acetonitrile at 3000 r.p.m. with a ramp of 1000 r.p.m. for 10 s, followed by another sintering step at 450 °C for 30 min. After cooling down to 150 °C the substrates were immediately transferred to a nitrogen atmosphere glove box for depositing the perovskite films.

**Planar  $SnO_2$  Substrate Preparation:**  $F:SnO_2$  substrates were first wiped with acetone and then cleaned for 10 min in piranha solution ( $H_2SO_4/H_2O_2 = 3:1$ ) followed by 10 min in a plasma cleaner prior to atomic layer deposition (ALD) (Savannah 100, Cambridge Nanotech).  $SnO_2$  was deposited at 118 °C using tetrakis(dimethylamino)-tin(IV) (TDMASn, 99.99%-Sn, Strem Chemicals INC., heated at 55 °C) and ozone at a constant growth rate of 0.065 nm per cycle measured by ellipsometry, which gives a film of  $\approx 15$  nm in thickness. Ozone was produced using an ozone generator (AC-2025, IN USA Incorporated) fed with oxygen gas (99.9995% pure, Carbagas) producing a concentration of 13% ozone in  $O_2$ . Nitrogen was used as a carrier gas (99.9999% pure, Carbagas) with a flow rate of 10 sccm.

**Perovskite Precursor Solution and Film Preparation:** The organic monovalent cation salts were purchased from Dyesol; the lead compounds

were purchased from TCI AMERICA. The following formulations were composed by mixing appropriate amounts of methylammonium iodide (MAI), ethylammonium iodide (EAI), guanidinium iodide (GAI), imidazolium iodide (IAI),  $PbI_2$ , MABr, EABr, GABr, IABr, and  $PbBr_2$ .

**MA/EA Perovskite:** Four perovskite solutions were prepared,  $MAPbI_3$  (containing 1.22 M MAI and 1.5 M  $PbI_2$  in anhydrous dimethylformamide (DMF):dimethyl sulfoxide (DMSO) 4:1 (v:v));  $EAPbI_3$  (containing 1.22 M EAI, 1.5 M  $PbI_2$  in anhydrous DMF:DMSO 4:1 (v:v));  $MAPbBr_3$  (containing 1.22 M MABr and 1.5 M  $PbBr_2$  in anhydrous DMF:DMSO 4:1 (v:v));  $EAPbBr_3$  (containing 1.22 M EABr and 1.5 M  $PbBr_2$  in anhydrous DMF:DMSO 4:1 (v:v)), then the four solutions are mixed to obtain the desired composition.

**MA/IA Perovskite:** Two perovskite solutions were prepared,  $MAPbI_3$  (containing 0.6 M MAI and 0.8 M  $PbI_2$  in anhydrous DMSO);  $IAPbI_3$  (containing 0.6 M IAI and 0.8 M  $PbI_2$  in anhydrous DMSO), then the two solutions are mixed to obtain the desired composition.

Two perovskite solutions were prepared,  $MAPbBr_3$  (containing 0.6 M MABr and 0.8 M  $PbBr_2$  in anhydrous DMSO);  $IAPbBr_3$  (containing 0.6 M IABr and 0.8 M  $PbBr_2$  in anhydrous DMSO), then the two solutions are mixed to obtain the desired composition.

**MA/GA Perovskite:** Two perovskite solutions were prepared,  $MAPbI_3$  (containing 0.6 M MAI and 0.8 M  $PbI_2$  in anhydrous DMSO);  $GAPbI_3$  (containing 0.6 M GAI and 0.8 M  $PbI_2$  in anhydrous DMSO), then the two solutions are mixed to obtain the desired composition.

Two perovskite solutions were prepared,  $MAPbBr_3$  (containing 0.6 M MABr and 0.8 M  $PbBr_2$  in anhydrous DMSO);  $GAPbBr_3$  (containing 0.6 M GABr and 0.8 M  $PbBr_2$  in anhydrous DMSO), then the two solutions are mixed to obtain the desired composition.

As reported previously by us,<sup>[4]</sup> the respective perovskite solution was spin coated on substrates, in a two-step procedure at 1000 and 6000 r.p.m. for 10 and 30 s, respectively. During the second step, 100  $\mu\text{L}$  of chlorobenzene was poured on the spinning substrate 15 s before the end of the procedure. The substrates were then annealed at 100 °C for 1 h in a nitrogen filled glove box.

**Hole Transporting Layer and Top Electrode:** After the perovskite annealing, the substrates were cooled down for a few minutes and a Spiro-OMeTAD (Merck) solution ( $70 \times 10^{-3}$  M in chlorobenzene) was spin-casted at 4000 r.p.m. for 20 s. Spiro-OMeTAD was doped with Li-TFSI (Sigma-Aldrich), tris(2-(1H-pyrazol-1-yl)-4-tert-butylpyridine)-cobalt(III) tris(bis(trifluoromethylsulfonyl)imide) (FK209, Dyenamo), and 4-tert-butylpyridine (TBP, Sigma-Aldrich). The molar ratio of additives for Spiro-OMeTAD was 0.5, 0.03, and 3.3 for Li-TFSI, FK209, and TBP, respectively. As the last step, 70–80 nm of gold top electrode was thermally evaporated through shadow masks under high vacuum.

**Perovskite Solar Cell Characterization:** Photovoltaic device testing of solar cells was measured using a 450 W xenon light source (Oriel). The spectral mismatch between AM1.5G and the simulated illumination was reduced by using a Schott K113 Tempax filter (Präzisions Glas and Optik GmbH). The light intensity was calibrated with an Si photodiode equipped with an infrared cutoff filter (KG3, Schott) and was recorded during each measurement. Current–voltage characteristics of the cells were obtained by applying an external voltage bias while measuring the current response with a digital sourcemeter (Keithley 2400). The voltage scan rate was  $10 \text{ mV s}^{-1}$  and no device preconditioning, such as prolonged light soaking or forward voltage bias, was applied before starting the measurement. The cells were masked with a black metal mask ( $0.16 \text{ cm}^2$ ) to fix the active area and reduce the influence of the scattered light.

SEM was used for morphological characterization on a ZEISS Merlin high-resolution (HR)-SEM.

The samples were analyzed by X-ray diffraction using a Bruker D8 Advance X-ray diffractometer using Cu K radiation ( $\lambda = 0.154178 \text{ nm}$ ) at a scanning rate of  $1^\circ \text{ s}^{-1}$  in the  $2\theta$  range from  $5^\circ$  to  $50^\circ$ .

UV–vis absorption measurements were performed on an Ocean Optics spectrophotometer HR-2000 c with deuterium and halogen lamps. In all measurements, a full spectrum from 300 to 800 nm points was sampled.

Steady state photoluminescence was measured using a Fluorolog, Horiba Jobon Yvon, FL-1065. A white tungsten lamp was used as a

luminous source. A monochromator was placed between the sample and the light source as well as between the sample and the detector. An excitation wavelength of 410 nm was used for MA<sub>(1-x)</sub>EA<sub>x</sub>PbBr<sub>3</sub> samples and 460 nm for the rest of the samples. The emission spectrum was measured from 10 nm higher than the emission spectrum to 850 nm in steps of one nm. An integration time of 1 s was used for each wavelength. Measurements were performed on perovskite films deposited on soda lime glass. The excitation source and the detector were placed at 90° with respect to each other. The sample was oriented 60° with respect to the excitation source in order to decrease interference from reflected light.

Electroluminescence measurements were performed using an LED setup. The devices were left unmasked, at room temperature and under constant nitrogen flow in order to prevent degradation during operation.

Electroluminescence yield was measured by applying either constant current or by applying varying potential to the device and by recording the emitted photon flux with a calibrated, large area (1 cm<sup>2</sup>) Si photodiode (Hamamatsu S1227-1010BQ) placed directly on top of the sample. The driving voltage or current was applied using a Bio-Logic SP300 potentiostat, which was also used to measure the short-circuit current of the detector at a second channel.

The IPCE spectra were measured under constant white light bias with an intensity of 10 mW cm<sup>-2</sup> supplied by an LED array. The superimposed monochromatic light was chopped at 2 Hz. The homemade system comprises a 300 W Xenon lamp (ICL Technology), a Gemini-180 double-monochromator with 1200 grooves per mm grating (Jobin Yvon Ltd) and a lock-in amplifier (SR830 DSP, Stanford Research System).

Stability measurements were performed as reported in ref. [2].

## Supporting Information

Supporting Information is available from the Wiley Online Library or from the author.

## Acknowledgements

S.G. gratefully acknowledges the Ministry of Science, Research and Technology of Iran and Iranian's National Elites Foundation and Iranian Nano Technology Initiative Council for financial support. M.S. acknowledges support from the cofunded Marie Skłodowska Curie fellowship, H2020 Grant Agreement No. 665667.

## Conflict of Interest

The authors declare no conflict of interest.

## Keywords

light-emitting devices, perovskite solar cells, quasi-3D cations, wide band-gap semiconductors

Received: April 10, 2017

Revised: July 17, 2017

Published online: August 18, 2017

- [1] R. E. Beal, D. J. Slotcavage, T. Leijtens, A. R. Bowring, R. A. Belisle, W. H. Nguyen, G. F. Burkhard, E. T. Hoke, M. D. McGehee, *J. Phys. Chem. Lett.* **2016**, *7*, 746.
- [2] M. Saliba, T. Matsui, K. Domanski, J.-Y. Seo, A. Ummadisingu, S. M. Zakeeruddin, J.-P. Correa-Baena, W. R. Tress, A. Abate, A. Hagfeldt, M. Grätzel, *Science* **2016**, *354*, 206.

- [3] N. K. Noel, S. D. Stranks, A. Abate, C. Wehrenfennig, S. Guarnera, A.-A. Haghighirad, A. Sadhanala, G. E. Eperon, S. K. Pathak, M. B. Johnston, A. Petrozza, L. M. Herz, H. J. Snaith, *Energy Environ. Sci.* **2014**, *7*, 3061.
- [4] M. Saliba, T. Matsui, J.-Y. Seo, K. Domanski, J.-P. Correa-Baena, M. K. Zakeeruddin, S. M. Zakeeruddin, W. Tress, A. Abate, A. Hagfeldt, M. Grätzel, *Energy Environ. Sci.* **2016**, *9*, 1989.
- [5] G. Kieslich, S. Sun, A. K. Cheetham, *Chem. Sci.* **2014**, *5*, 4712.
- [6] L. Protesescu, S. Yakunin, M. I. Bodnarchuk, F. Krieg, R. Caputo, C. H. Hendon, R. X. Yang, A. Walsh, M. V. Kovalenko, *Nano Lett.* **2015**, *15*, 3692.
- [7] E. Edri, S. Kirmayer, M. Kulbak, G. Hodes, D. Cahen, *J. Phys. Chem. Lett.* **2014**, *5*, 429.
- [8] V. M. Goldschmidt, *Naturwissenschaften* **1926**, *14*, 477.
- [9] M. R. Filip, G. E. Eperon, H. J. Snaith, F. Giustino, *Nat. Commun.* **2014**, *5*, 5757.
- [10] G. E. Eperon, G. M. Paternò, R. J. Sutton, A. Zampetti, A. A. Haghighirad, F. Cacialli, H. J. Snaith, *J. Mater. Chem. A* **2015**, *3*, 19688.
- [11] D. M. Nicholas, Z. Huanping, C. Qi, S. Pengyu, L. Zonghao, M. Lei, Y. En-Ping, S. Andy, Y. Yang, *Nano Lett.* **2016**, *16*, 1009.
- [12] C. Quarti, E. Mosconi, F. De Angelis, *Chem. Mater.* **2014**, *26*, 6557.
- [13] J.-W. Lee, D.-H. Kim, H.-S. Kim, S.-W. Seo, S. M. Cho, N.-G. Park, *Adv. Energy Mater.* **2015**, *5*, 1501310.
- [14] N. Q. Li, Y. Mingjian, C. Riccardo, V. Oleksandr, M. B. Eric, H. Sjoerd, B. Andrei, R. K. Ahmad, Z. Kui, A. Aram, H. K. Dong, H. S. Edward, *J. Am. Chem. Soc.* **2016**, *138*, 2649.
- [15] G. E. Eperon, S. D. Stranks, C. Menelaou, M. B. Johnston, L. M. Herz, H. J. Snaith, *Energy Environ. Sci.* **2014**, *7*, 982.
- [16] F. C. Hanusch, E. Wiesenmayer, E. Mankel, A. Binek, P. Angloher, C. Fraunhofer, N. Giesbrecht, J. M. Feckl, W. Jaegermann, D. Johrendt, T. Bein, P. Docampo, *J. Phys. Chem. Lett.* **2014**, *5*, 2791.
- [17] W. Peng, X. Miao, V. Adinolfi, E. Alarousu, O. El Tall, A.-H. Emwas, C. Zhao, G. Walters, J. Liu, O. Ouellette, J. Pan, B. Murali, E. H. Sargent, O. F. Mohammed, O. M. Bakr, *Angew. Chem. Int. Ed.* **2016**, *55*, 10686.
- [18] T. J. Jacobsson, J.-P. Correa-Baena, M. Pazoki, M. Saliba, K. Schenk, M. Grätzel, A. Hagfeldt, *Energy Environ. Sci.* **2016**, *9*, 1706.
- [19] D. Ma, Y. Fu, L. Dang, J. Zhai, I. A. Guzei, S. Jin, *Nano Res.* **2017**, *10*, 2117.
- [20] Z. Yuan, Y. Yang, Z. Wu, S. Bai, W. Xu, T. Song, X. Gao, F. Gao, B. Sun, *ACS Appl. Mater. Interfaces* **2016**, *8*, 34446.
- [21] M. Mittal, A. Jana, S. Sarkar, P. Mahadevan, S. Sapra, *J. Phys. Chem. Lett.* **2016**, *7*, 3270.
- [22] M. A. Green, A. Ho-Baillie, H. J. Snaith, *Nat. Photonics* **2014**, *8*, 506.
- [23] C. C. Stoumpos, D. H. Cao, D. J. Clark, J. Young, J. M. Rondinelli, J. I. Jang, J. T. Hupp, M. G. Kanatzidis, *Chem. Mater.* **2016**, *28*, 2852.
- [24] T. J. Jacobsson, J.-P. Correa-Baena, E. Halvani Anaraki, B. Philippe, S. D. Stranks, M. E. F. Bouduban, W. Tress, K. Schenk, J. Teuscher, J.-E. Moser, H. Rensmo, A. Hagfeldt, *J. Am. Chem. Soc.* **2016**, *138*, 10331.
- [25] B. Philippe, M. Saliba, J.-P. Correa-Baena, U. B. Cappel, S.-H. Turren-Cruz, M. Grätzel, A. Hagfeldt, H. Rensmo, *Chem. Mater.* **2017**, *29*, 3589.
- [26] M. A. Green, *Prog. Photovoltaics Res. Appl.* **2012**, *20*, 472.
- [27] H. J. Snaith, *J. Phys. Chem. Lett.* **2013**, *4*, 3623.
- [28] J.-W. Schüttauf, M. A. Modestino, E. Chinello, D. Lambalet, A. Delfino, D. Dominé, A. Faes, M. Despeisse, J. Bailat, D. Psaltis, C. Moser, C. Ballif, *J. Electrochem. Soc.* **2016**, *163*, F1177.
- [29] W. Tress, N. Marinova, T. Moehl, S. M. Zakeeruddin, M. K. Zakeeruddin, M. Grätzel, *Energy Environ. Sci.* **2015**, *8*, 995.
- [30] W. Tress, N. Marinova, O. Inganäs, M. K. Zakeeruddin, S. M. Zakeeruddin, M. Graetzel, *Adv. Energy Mater.* **2015**, *5*, 1400812.
- [31] F. Giordano, A. Abate, J. P. Correa Baena, M. Saliba, T. Matsui, S. H. Im, S. M. Zakeeruddin, M. K. Zakeeruddin, A. Hagfeldt, M. Graetzel, *Nat. Commun.* **2016**, *7*, 10379.